Toward constraint of ionization-potential depression models in a convergent geometry

D. T. Bishel[a,b,*], P. M. Nilson[b], D. A. Chin[a,b], J. J. Ruby[c], E. Smith[a,b], S. X. Hu[b], R. Epstein[b], I. E. Golovkin[d], J. R. Rygg[a,b,e], G. W. Collins[a,b,e]

[a]*Department of Physics and Astronomy, University of Rochester, Rochester, New York 14627, USA*
[b]*Laboratory for Laser Energetics, University of Rochester, Rochester, New York 14623, USA*
[c]*Lawrence Livermore National Laboratory, Livermore, California 94550, USA*
[d]*Prism Computational Sciences, Madison, Wisconsin 53711, USA*
[e]*Department of Mechanical Energy, University of Rochester, Rochester, New York 14627, USA*

Abstract

We demonstrate the value of inner-shell x-ray absorption spectroscopy for dense-plasma atomic physics and explore the coupling between constraint of the thermodynamic state and constraint of ionization-potential depression models. Synthetic K-shell absorption spectra are generated along a radius from a point-like core and analyzed using different ionization-potential depression models. Within this synthetic analysis framework, we identify plasma conditions (T_e = 400 eV, ρ = 40g/cm^3) accessible by spherical implosions where K-shell absorption spectra discriminate between models if the material temperature is measured to a precision of 20%. The analysis is extensible to a finite-sized core and can be used to guide future studies of ionization-potential depression, informing material and radiative properties of matter in fusion plasmas and stellar interiors.

Keywords: continuum lowering, opacity, x-ray absorption spectroscopy, ionization balance, Bayesian inference

1. Introduction

Understanding how atoms emit and absorb radiation in dense plasmas is a substantial challenge of modern science [1]. At sufficiently high densities, plasma electrons can screen the nuclear attraction of bound electrons and reduce their binding energy [2]. Additionally, atomic orbitals become substantially modified by nearby ions [3, 4], even to such a degree that exotic interspecies radiative transitions may occur [5]. Quantitative measurements of these processes test our understanding of fundamental atomic physics and are critical for modeling the radiative energy transport of fusion plasmas on Earth and the evolution and structure of stars [6–9]. Many of the experiments probing atomic physics in dense plasmas, however, are performed in planar geometries, which are currently limited to conditions within a few factors of solid density [10–12]. This lack of data at high densities impedes the development of accurate descriptions of dense plasmas.

Spherical implosions contain a potential benefit to the field of dense-plasma atomic physics that has yet to be fully exploited. Leveraging pressure amplification through convergence, implosions produce the highest densities achievable in the laboratory, with some designs exceeding 1000 g/cm^3 [13]. The benefits of higher densities to atomic physics are manifold. Testing theoretical models across a greater region of parameter space will provide the data needed for global descriptions of dense plasmas. In this way, the extreme densities accessed by implosions complement studies of atomic physics at conditions nearer to solid density [10–12, 14–16]. Second, the discrepancy between competing models can increase at high densities, offering the experimentalist greater leverage when comparing models to data. Furthermore, implosions offer a unique method for assembling and studying dense plasmas. The study of dense-plasma phenomena in an independent platform can corroborate conclusions of other studies, establish the scientific reproducibility of an experimental result, or identify systematic uncertainties unique to a given method. Finally, novel emission and absorption pathways enabled by interspecies radiative

*Corresponding author
Email address: dbishel@ur.rochester.edu (D. T. Bishel)

transitions have been predicted to emerge at densities at and above 100 g/cm^3 [5] — conditions not accessible in planar geometries.

Implosions present an interesting though challenging environment from a measurement perspective. The necessarily high densities require penetrating diagnostics of both the plasma conditions and the atomic physics of the sample, excluding many traditional probes of temperature or density. The line-of-sight integration of a penetrating diagnostic complicates its interpretation. The exiting radiance depends on the radiative properties and thermodynamic states along a chord through the assumed spherically symmetric, radially varying plasma. The ability to forward model the exiting radiance and thus assess the accuracy of atomic models is influenced by our knowledge of the hydrodynamic and thermodynamic evolution.

Although the integrated nature of implosions couples together uncertainties from hydrodynamic, thermodynamic, and atomic physics models, this coupling allows constraint of one of these seemingly disparate models by direct measurement of another. Advanced statistical techniques are required to exploit the coupling between models. For instance, a Bayesian inference framework has been used to infer the implosion hot-spot pressure (a thermodynamic quantity) by measurement of the explosion-phase trajectory of the shell (a hydrodynamic quantity) [17, 18]; knowledge of the hot-spot pressure then constrains energy balance and implosion models. Similarly, a synthetic study of the interplay between atomic physics and other models can identify the experimental conditions and diagnostic suite needed to constrain atomic physics models. Experiments can then be designed that access the optimal conditions for informing models, while optimizing the use of valuable experimental time.

In this work, we demonstrate the value of inner-shell x-ray absorption spectroscopy for dense-plasma atomic physics and explore the coupling between constraint of the thermodynamic state and constraint of ionization potential depression (IPD) models. We also develop an analysis framework that quantifies the precision of thermodynamic state measurements required to discriminate between IPD models. In Sec. 2, we provide a brief summary of IPD models and motivate the use of $1s-2p$ absorption spectroscopy of L-shell ions as a means to discriminate between IPD models. In Sec. 3, synthetic K-shell absorption spectra are generated along a radius from a point-like core and analyzed assuming different IPD models. We identify plasma conditions accessible in spherical implosions where measurement of the plasma temperature within 20% fractional uncertainty discriminates between models. This example can help guide future studies of IPD in dense matter.

2. Constraint of IPD by K-shell absorption spectroscopy

As a tractable example of implosion-relevant atomic physics, we consider the impact of ionization potential depression (IPD) models on ionization and its manifestation in the observed K-shell absorption spectrum. This will define the model explored in Sec. 3. Furthermore, to enable discrimination between competing IPD models, we identify conditions that produce a measurable difference in the observed spectrum between models.

The Stewart–Pyatt (SP) [19] and Ecker–Kröll (EK) [20] models of IPD describe the electrostatic interaction between an ion and the plasma environment. The ground-state free-energy contribution of the plasma increases the ionization state of material at high densities. These models have been used for over half a century and are incorporated into the equations of state used in radiation-hydrodynamic codes commonly used by the high-energy-density-physics community [21, 22]. However, recent experiments have revealed inconsistencies in these models [11, 12], renewing interest in their study and the pursuit of self-consistent models [14, 15, 23, 24]. Density-functional-theory–based models [25, 26] of dense plasmas offer a more-complete description of the plasma environment, but still introduce model uncertainty through the approximations inherent in the choice of the exchange-correlation potential [27]. Due to the lack of well-constrained experimental data, tests of such models have predominantly been limited to within a few factors of solid density of the material under study [10–12, 14–16]. Data at higher densities are critically needed to discriminate between these competing descriptions of dense matter.

The IPD ΔE_c is an effective reduction in the ionization potential χ_j, emerging due to the electrostatic interaction between an ion and the circumfluent dense plasma in a chemical-equilibrium picture of ionization [20]. Under the assumption of local thermodynamic equilibrium (LTE), the ratio of ion densities N_j and N_{j+1} of neighboring ionization states j and $j+1$ is

$$\frac{N_{j+1}N_\mathrm{e}}{N_j} = 2\left(\frac{2\pi m_\mathrm{e} k T_\mathrm{e}}{h^2}\right)^{3/2}\frac{\mathcal{Z}_{j+1}}{\mathcal{Z}_j}\exp\!\left(-\frac{\chi_j-\Delta E_\mathrm{c}}{kT_\mathrm{e}}\right), \quad (1)$$

with free electron number density N_e, electron mass m_e, Planck constant h, Boltzmann constant k, plasma temperature T_e, and internal partition function $\mathcal{Z}_j$ of ion j. At the high densities where IPD manifests, the high collision frequency between free and bound electrons tends

Figure 1: (a) Mean ionization $\bar{Z}$ of Cr ($Z = 24$) predicted by the screened hydrogenic model with a Stewart–Pyatt IPD model. (b) Difference in $\bar{Z}$ between Ecker–Kroll and Stewart–Pyatt IPD models. Numerical noise due to convergence is visible in regions of low ionization. Dashed contours indicate the He- and Ne-like states that bound L-shell ionization states using the Stewart–Pyatt IPD model. As denoted by the grey line, implosions can be designed to drive a Cr witness layer into L-shell average ionization states during stagnation; see Sec. 3 for further details. Open circles in (b) denote the conditions referenced in Fig. 6.

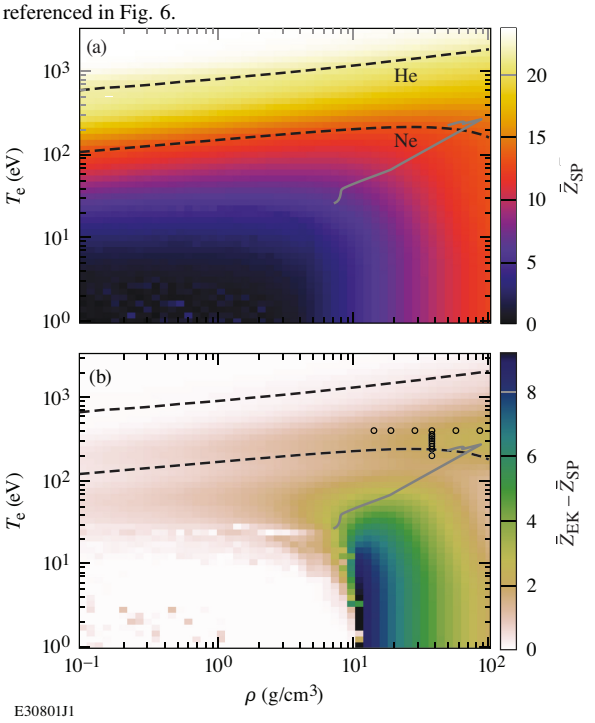

to establish LTE among level populations. To estimate where LTE is valid, we use the approximate validity criterion of Griem [28]

$$N_e \gtrsim 3.9 \times 10^{17} z^7 \left(\frac{kT}{z^2 E_H}\right)^{1/2} \left(\frac{4E_2}{3z^2 E_H}\right)^3 [\mathrm{cm}^{-3}], \quad (2)$$

with temperature kT in eV, $E_H = 13.6$ eV, E_2 the excitation energy of the resonant transition, and ion charge z. For $kT = 400$ eV and $z = 21$ (Li-like Cr), E_2 corresponds to an $n = 3$ to $n = 2$ transition of roughly 900 eV (see Fig. 2), and $N_e \gtrsim 1.5 \times 10^{24}$ cm^3, or $\rho \gtrsim 6$ g/cm^{-3}. As will be shown, the relevant conditions are a factor of two more dense.

ΔE_c and its impact on the mean ionization state $\bar{Z}$ can be calculated with a screened-hydrogenic average-ion model [6, 29, 30]. This simplified atomic model treats electron correlations through screening coefficients. Shell populations, mean ionization $\bar{Z}$, and IPD are calculated self-consistently at a given plasma temperature and mass density.[1] Hydrogenic equations modified by the screening can be employed to calculate level energies, oscillator strengths, excitation rates, and other atomic data. As such, the model is approximate yet computationally inexpensive, and a wide range of parameter space can be quickly surveyed to identify where more-accurate, computationally expensive codes should be deployed. In terms of discriminating between IPD models, the model is of high utility, since it allows interrogating the difference caused by IPD within a well-defined (although approximate) model. Additional details are provided in the appendix.

Within the average-ion model, the magnitude of IPD for the Ecker–Kröll and Stewart–Pyatt models is evaluated according to [16]

$$\Delta E_c^{\mathrm{EK}} = \frac{(\bar{Z}+1)^{4/3}}{R_{\mathrm{IS}}/a_0} \times 27.2 \text{ eV} \quad (3)$$

$$\Delta E_c^{\mathrm{SP}} = \frac{3}{2}\frac{\bar{Z}+1}{R_{\mathrm{IS}}/a_0} \times 27.2 \text{ eV}, \quad (4)$$

where $R_{\mathrm{IS}} = (\frac{4\pi N_i}{3})^{-1/3}$ is the ion-sphere radius computed at total ion density N_i, and a_0 is the Bohr radius. The ion-sphere limit used for Stewart–Pyatt is valid for $(\frac{R_{IS}}{\lambda_D})^3 >> 1$, with Debye length $\lambda_D = [\frac{4\pi e^2}{kT_e}(\bar{Z}+1)\, n_e]^{-1/2}$. To provide numerical values, we consider chromium (Cr, $Z = 24$) as a representative mid-Z element. The resulting $\bar{Z}$ assuming ΔE_c^{SP} is shown in Fig. 1(a). Ionization occurs with both increasing temperature (thermal ionization) and increasing density due to increasing IPD (pressure ionization). The dashed contours bound the region where Cr exists in an L-shell average ionization state. Figure 1(b) shows the difference in $\bar{Z}$ between EK and SP. Density and temperature states in the vicinity of 40 g/cm^3 and 400 eV tend to produce differences in $\bar{Z}$ exceeding one ionization state.

To discriminate between IPD models, an experimental constraint of $\bar{Z}$ is required. The ionization balance is encoded in the ionization-state–dependent energy hν of the $1s - np$ transitions. Additionally, the high photon energies near 6 keV and long inverse-Bremsstrahlung attenuation lengths of these inner-shell transitions are beneficial properties for diagnostics of dense plasmas, since the associated spectrum can transmit through the dense plasma environment to reach an external detector.

The screened-hydrogenic average-ion model can be used to estimate the transition energy hν between shells

[1] The average ion model is fundamentally a plasma physics model. The $\bar{Z}$ that it predicts will not recover the electron carrier density of ambient metals.

Figure 2: Energies of $n = 1-2$ (orange) and $n = 1-3$ (blue) transitions in Cr as a function of ionization state from the screened-hydrogenic average-ion model with a Stewart–Pyatt IPD. Vertical dashed lines denote the closed-shell configurations of Ar-like, Ne-like, and He-like. Horizontal dashed lines denote the K_α and K_β energies. Transition energies increase substantially when ionizing through the L shell. Trends are unaffected by choice of IPD model. For most charge states the difference in transition energy lies within one standard deviation; only Ne- and F-like differ by two standard deviations.

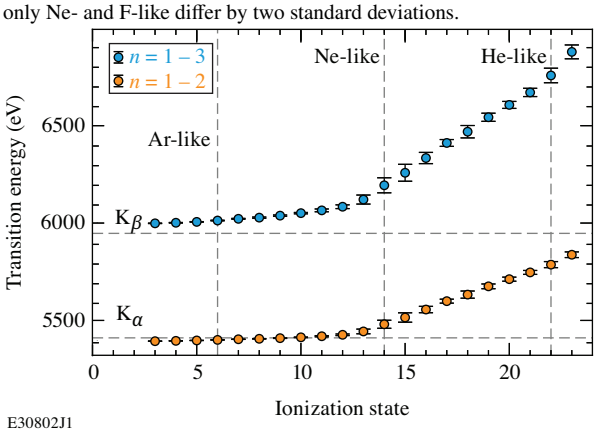

of different principal quantum numbers n as a function of T_e and ρ. The model conceives a fictitious ion with non-integer ionization state $\bar{Z}$ to represent the average ionization state of an ensemble of ions in thermodynamic equilibrium. To estimate hν as a function of a realistic integer ionization state Z_j, we construct a histogram of all transitions having ionization $\bar{Z}$ between $Z_j - 1/2$ and $Z_j + 1/2$, and assign this distribution of hν to the ionization state Z_j. We repeat this for each transition ($n = 1 - 2$ and $n = 1 - 3$) and each ionization state Z_j from the neutral atom ($Z_j = 0$) to the hydrogenic state ($Z_j = Z-1$). Because of the simplified treatment of electron correlations and the lack of angular-momentum splitting, the absolute hν are approximate, but the model captures the change of hν with increasing ionization.

The resulting hν for $n = 1-2$ and $n = 1-3$ transitions are shown in Fig. 2. Error bars represent the standard deviation of each hν distribution and convey the range of hν that a given transition can assume. A large shift in both the $n = 1-2$ and $n = 1-3$ transition energies is observed with increasing ionization for L-shell ionization states. These shifts are large enough to be resolved by a moderate-resolution spectrometer $E/\Delta E \approx 200$. Requiring an L-shell ionization state (c.f. contours in Fig. 1) excludes the region of largest ionization difference for Cr at densities above 10 g/cm^3 and temperatures below 50 eV, but still admits a region of a few hundred eV and tens of g/cm^3 where $\bar{Z}^{EK} - \bar{Z}^{SP} \approx 3$. Given that contributions of individual ionization states are observable in the $1s - 2p$ spectrum, a difference of three ionization states is easy to discern.

The $1s - 2p$ transitions of L-shell ions typically manifest as line absorption when observed in a backlighting geometry. The lack of $1s$ vacancies in the ground state of L-shell configurations results in weak $1s - 2p$ emission because such emission can only occur after nonequilibrium pumping (e.g., photoionization) of a $1s$ vacancy. However, the $2p$ vacancies present in ground-state L-shell ions will admit $1s - np$ absorption transitions for $n \geq 2$. The $1s - 2p$ line absorption spectrum from L-shell ions constitutes a measurement of the ionization distribution and a constraint of IPD models in dense plasmas.

We note that there exists a region of large difference in $\bar{Z}$ for $\rho \approx 10$ g/cm^3 and $T < 10$ eV. However, for this region of $\bar{Z} < 14$, the $1-2$ and $1-3$ transition energies change little with ionization. Inferring $\bar{Z}$ from these transitions involves interpreting merged lines, introducing model uncertainty because a greater-than-expected transition energy for a given ionization state is indistinguishable from greater ionization. Though there have been efforts to accurately model the $1s - 2p$ transitions of weakly ionized species [31], we avoid this uncertainty by considering the more readily-interpretable K-shell absorption of L-shell ionization states.

3. Discriminating between IPD models

3.1. Hydrodynamic simulations of implosions

Implosions can be designed to access conditions where $1s - 2p$ absorption in L-shell Cr is sensitive to the choice of IPD model. Previous experiments have demonstrated the ability to produce $1s - 2p$ absorption spectra in a variety of mid-Z layers in implosion shells [32–35].

In a direct-drive implosion, laser ablation of the exterior layers of the implosion shell establishes a pressure of a few TPa [36] that accelerates the remaining shell mass toward the capsule center. After accelerating to hundreds of kilometers per second, the remaining shell mass performs compressive work on the gas-filled core, rapidly heating and compressing the gas. At this time, the gas not only emits a bright, broadband x-ray spectrum, but also performs compressive work on the plastic shell, launching a return shock outward through the shell that heats and compresses the shell material as it propagates. The x-ray radiation from the stagnated

core is thus naturally co-timed to the shell compression, eliminating the need for an external x-ray source to probe the atomic state of the shock-compressed shell.

We now consider the thermodynamic states accessed by a Cr witness layer embedded in an implosion shell. Figure 3(a) shows a laser pulse shape and target geometry with a submicron Cr layer embedded in a plastic (CH) shell. The Cr layer is kept thin to reduce gradients across the Cr during measurement while limiting its optical depth [32]. An Ar dopant in the core increases the brightness of the stagnation continuum flash without producing line emission in the spectral range near the Cr $1s-2p$ absorption. Use of a thick, low-Z CH shell drastically reduces hydrodynamic instability growth compared to high neutron-yield inertial-confinement-fusion implosions, while lowering the optical depth of the capsule in the spectral range of interest.

Figures 3(b) and 3(c) show the conditions accessed by the Cr layer and gas core of this capsule near peak compression, as simulated by the 1-D radiation-hydrodynamics code *LILAC* [21]. The Cr layer is expected to exceed temperatures of 200 eV, where IPD-dependent $\bar{Z}$ predictions diverge (see grey line in Fig. 1). Simultaneously, the hot Ar-doped core produces a bright x-ray continuum in the spectral range around the Cr $1s-2p$ transition energy, acting as a backlighter for an absorption spectrum of the compressed Cr. Figure 3(d) shows the evolution of the radiance exiting the core and inner CH layer, calculated from the *LILAC* simulations and integrated over the spectral range of 5 to 7 keV. Tabulated emissivities and opacities were used [37]. This x-ray emission backlights the shell and makes possible $1s-2p$ absorption spectroscopy of the compressed Cr at temperatures above 100 eV and densities around 40 g/cm^3.

Figure 3: (a) Geometry and laser pulse shape used in 1-D *LILAC* radiation-hydrodynamic simulations. Simulated temperature (red) and density (blue) averaged over (b) the Cr layer and (c) the D_2–Ar core plotted as a function of time during stagnation. Colored bands indicate the ranges of temperature and density across the given layer. (d) Radiance emitted by the core and inner CH layer in the spectral range of 5 to 7 keV, calculated by post-processing *LILAC* radial profiles. Emission persists after the Cr is heated by the return shock, backlighting the ionized Cr and enabling absorption spectroscopy.

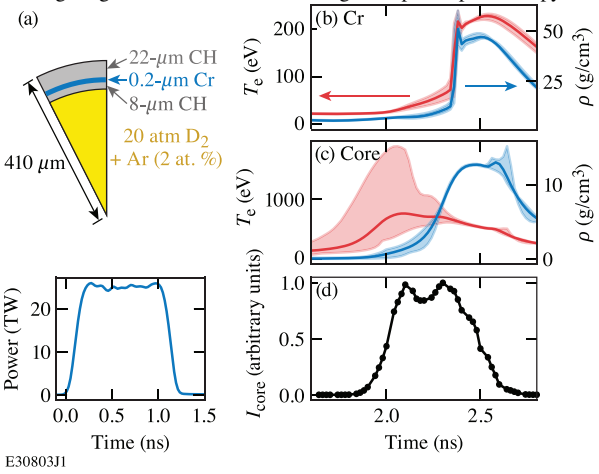

3.2. *Radiative transport model*

To quantitatively determine how IPD models influence an observable spectrum, we simplify the implosion into a backlit slab geometry. We consider only a backlit slab because the effects of the implosion geometry on the transmitted spectra has been explored previously, including line-of-sight effects [38], mix [39, 40], and gradients [40]. The model system consists of a Planckian spectrum B_ν of temperature T_r incident on a homogeneous slab of material with temperature T_e, mass density ρ, and thickness ℓ. This is akin to having an optically thick point-like core, optically thin CH layers, and negligible limb-brightening of the shell at the photon energies of interest. The collisional-radiative spectral modeling code *PrismSPECT* [41] is used to calculate the emission and linear attenuation coefficients $j_\nu(T_\mathrm{e},\rho)$ and $\alpha_\nu(T_\mathrm{e},\rho)$ of Cr in the spectral range of the $1s-2p$ absorption feature (5300 eV $< h\nu <$ 5800 eV). j_ν and α_ν are functions of the ionization states present at a given temperature and density, and therefore depend on the IPD model used. The transmitted spectral radiance (or specific intensity) I_ν is given by the solution to the equation of radiative transfer in one dimension,

$$I_\nu = B_\nu(T_\mathrm{r})e^{-\alpha_\nu \ell} + \frac{j_\nu}{\alpha_\nu}\left(1 - e^{-\alpha_\nu \ell}\right), \qquad (5)$$

where the explicit dependence of j_ν and α_ν on ρ and T_e has been suppressed.

To determine the sensitivity of the inferred thermodynamic state to the choice of the atomic physics model, we analyze a single synthetic spectrum with different IPD models. We use Eq. 5 as our model, plus an additive constant to simulate background and a multiplicative constant to simulate unknown detector gain:

$$I_\nu = G \times \left[B_\nu(T_\mathrm{r})e^{-\alpha_\nu \ell} + \frac{j_\nu}{\alpha_\nu}\left(1 - e^{-\alpha_\nu \ell}\right)\right] + C. \qquad (6)$$

The model contains six free parameters: core radiation temperature T_r, slab temperature T_e, slab density ρ, slab thickness ℓ, background signal C, and gain G.

We restrict our analysis to the coupling of uncertainty between the thermodynamic state of the plasma and the

choice of atomic model, and therefore do not model any systematic or random uncertainties associated with the spectrometer or detector beyond a multiplicative constant. Noise on I_ν is not generated but could be done for each photon energy bin by sampling I_ν from a probability distribution representative of the diagnostic noise characteristics.

The atomic physics model yielding $\alpha_\nu(T_\mathrm{e}, \rho)$ and $j_\nu(T_\mathrm{e}, \rho)$ requires the choice of an IPD model, either EK or SP. The spectrum being analyzed, which we will refer to as the "synthetic data," is generated from Eq. 6 with known true values of each of the parameters, including the choice of IPD model to determine j_ν and α_ν. EK is used to generate the synthetic data and is the true IPD model in all cases considered. To systematically track correlations among all parameters and explicitly incorporate prior knowledge into parameter estimates, Bayesian inference [42] with a Gaussian likelihood function is performed on the synthetic data using the model of Eq. 6. Uniform prior distributions for each of the six free parameters were chosen to be wide enough to not truncate the posterior distributions. A Pyro-based sampler was used to explore the Gaussian likelihood [43, 44]. The inference was performed once for each IPD model, resulting in one set of posterior distributions for each of EK and SP.

This analysis leverages the relationship between IPD and the ionization balance encoded in the j_ν and α_ν. Previous IPD studies have focused on other consequences of IPD, including the reduction in the photoionization energy of core electrons [12] and the delocalization of upper-state orbitals [11]. Other studies have provided indirect evidence for particular IPD models by matching experimental observables to IPD-dependent results of radiation-hydrodynamic simulations [14, 35]. This latter class of study assumes that plasma conditions are known and determines how well different models reproduce some observable. We instead take a forward-modeling approach, identifying the conditions that different models require to reproduce the observed absorption spectrum. This approach decouples our analysis from computationally expensive hydrodynamic simulations.

3.3. Inference and model comparison

Synthetic data were generated using the parameters in Table 1. Uncertainty of the measurements was assumed to be 5% of the maximum I_ν value in the range of the spectrum considered. This corresponds to an ideal case in which the spectrometer and detector do not contribute to the signal variance [35]. Figure 4 shows the 90% highest-density intervals (HDIs) of the EK and SP posterior predictive distributions. Both models are capable of producing reasonable fits to the synthetic data. This is because *PrismSPECT*'s implementation of IPD only modifies the state populations and ionization potentials in the atomic kinetics calculation, and does not affect the atomic structure, transition energies, or oscillator strengths. In general, the ability of a model to reproduce observed spectra is insufficient evidence for the model's validity.

Figure 5 shows contours of the posterior distributions of the model parameters for EK and SP corresponding to the posterior predictives of Fig. 4. First, the EK model accurately captures the true parameter values used to generate the synthetic data. This is expected, since EK was the true model for the synthetic data, yet it is still an important demonstration in establishing an accurate analysis method. Second, the two IPD models yield posterior distributions of T_e which are mutually exclusive. To discriminate between the models, the precision of an experimental measurement of temperature must be good enough such that its probability density distribution coincides with only one of the model posteriors. The more exclusive the model posteriors at the given conditions, the less precise an experimental measurement needs to be in order to discriminate between the models. For this idealized geometry, the 90% HDI of an accurate temperature measurement must lie within roughly 20% of the true value to exclude a majority of the SP posterior and favor the true EK posterior. Inferred values of the plasma parameters of ρ, T_r, and ℓ are only modestly influenced by the choice of IPD model, and their measurement in an experiment would not substantially improve our ability to discriminate between the two models.

The inference's ability to discriminate between IPD models is directly related to the difference in predicted $\bar{Z}$. To demonstrate this, we have repeated the synthetic

Table 1: True parameter values used to generate synthetic data of Figs. 4 and 5.

Quantity	Parameter	Value
Radiation temperature	T_r	600 eV
Cr temperature	T_e	400 eV
Cr density	ρ	40 g/cm^3
Cr thickness	ℓ	10^{-6} cm
Background	C	0.03 J/s/m^2/sr/Hz
Gain	G	1
IPD model	None	Ecker–Kröll

Figure 4: (a) Backlit slab geometry used to generate and analyze synthetic spectra. Posterior predictive distributions of the (b) Ecker–Kröll and (c) Stewart–Pyatt IPD models plotted over synthetic spectra (black points) using the parameters listed in Table 1. The 90% HDI is shown by the colored bands. Stewart–Pyatt can accurately represent the Ecker–Kröll–simulated spectrum, but gives statistically different temperature-density conditions (see Fig. 5).

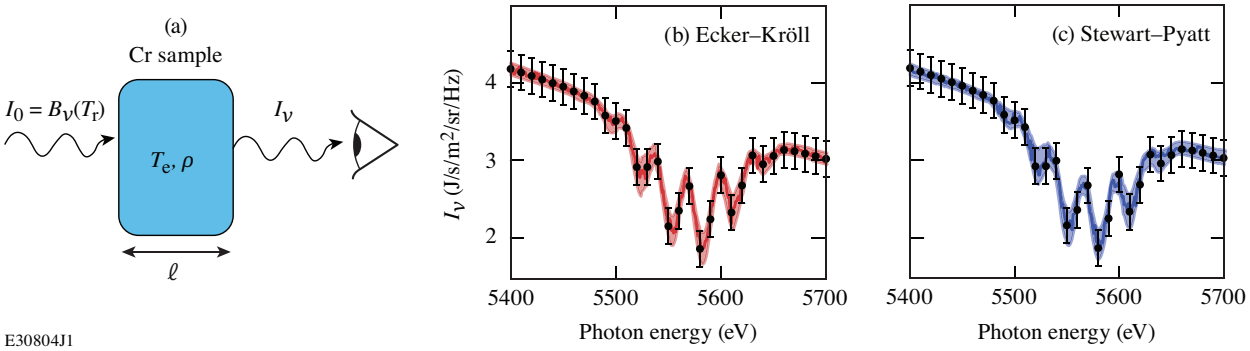

Figure 5: (a) Single-parameter and (b) joint posterior probability distributions of a subset of the model parameters, corresponding to the posterior predictive distributions of Ecker–Kröll (red) and Stewart–Pyatt (blue) in Fig. 4. Values used to generate the spectra are indicated in (a) by vertical dashed lines and in (b) by open black circles. The two models require statistically different temperature-density conditions to match the synthetic spectra.

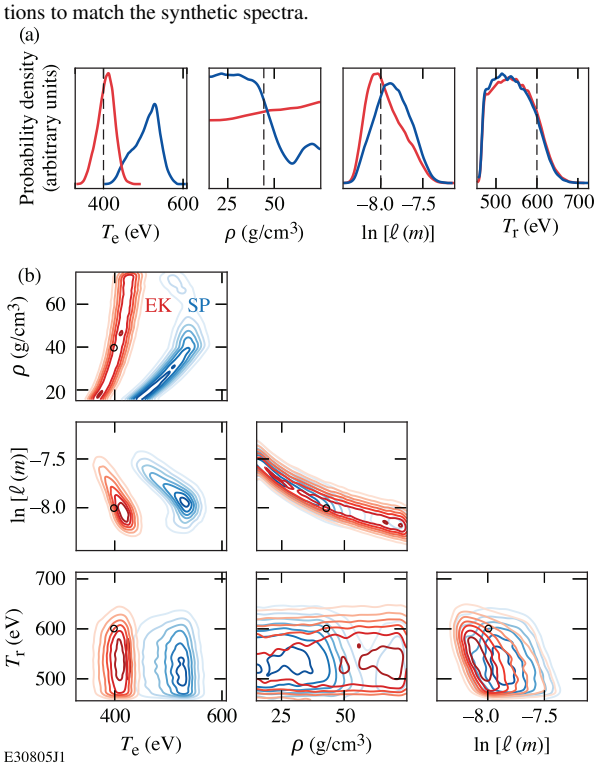

analysis at other T_e and ρ conditions. The other model parameters listed in Table 1 were not changed. Cases were chosen to cover a range of predicted differences in $\bar{Z}$ [see open circles in Fig. 1(b)]. The difference in $\bar{Z}$ between the IPD models tends to increase with increasing temperature and density. The mean and 90% HDIs of the inferred posterior distributions of temperature are shown in Fig. 6. As was the case in the previous example, only temperature offers leverage to discriminate between models. The cases which possess greater differences in $\bar{Z}$ between the IPD models (here, higher T_e and ρ) also yield greater divergence in inferred temperatures. These cases would have a correspondingly more lenient requirement on the uncertainty of an experimental temperature measurement.

Addition of a spectroscopic thermometer that does not rely on the ionization balance would enable discrimination between models. While the ionization balance is affected by IPD (see Eq. 1), excitation balances are not affected by IPD and could constitute an independent measure of temperature. By doping the witness with a lower-Z species, which ionizes to a K-shell charge state at the achieved conditions, one could simultaneously measure higher-series $1s-np$ emission lines from a single ionization state of the dopant and extract a temperature from the corresponding line ratios (e.g. of He-like $1s-2p$ and He-like $1s-3p$). Care must be taken to ensure that the lower-energy line emission of the lower-Z species is still penetrating enough to escape the dense plasma environment to be useful for measurement. Additionally, there is value in doping with a species similar in Z to constrain the Z-scaling of the IPD [15].

Figure 6: Mean and 90% HDIs of temperatures inferred by EK (red) and SP (blue). Synthetic data were generated at (a) varying temperatures and 40 g/cm^3 and (b) varying densities and 400 eV. Posterior distributions become increasingly exclusive with higher temperature and density, corresponding to conditions where EK and SP predict increasingly different $\bar{Z}$.

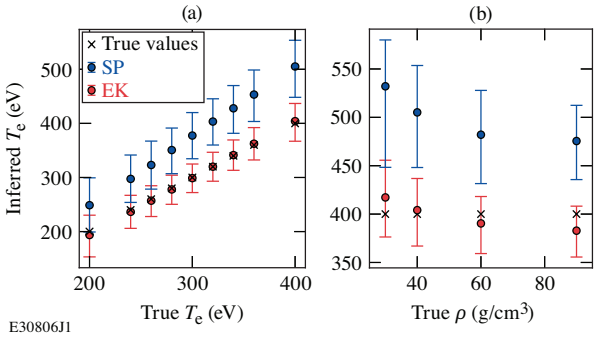

4. Conclusion

Extreme drivers are required to access the extreme conditions relevant to stellar interiors and fusion plasmas. Spherical implosions are an attractive option for their ability to assemble dense matter and simultaneously probe its material properties. To guide future IPD studies in implosions, we have demonstrated that $1s-2p$ absorption spectra of L-shell ions can discriminate between the Ecker–Kröll and Stewart–Pyatt IPD models by experimentally constraining the ionization distribution. In the cases considered, higher compression leads to a greater ability to discriminate between IPD models, further motivating the pursuit of measurements at higher densities.

The framework we have presented can be extended to quantitatively study the interplay between diagnostic performance and physics inference. Spectral resolution, detector noise characteristics, and thermodynamic gradients can degrade the inference by either increasing measurement uncertainty or increasing the number of parameters required to represent the thermodynamic states. Future work includes determining the impact of these experimental realities on the ability to discriminate between models. Additionally, other atomic models such as density-functional theory can be compared to identify the set of models consistent with a given measurement.

Implosions are an underutilized resource for studying atomic physics of dense plasmas, since they produce the highest density conditions achievable in the laboratory. Methods are emerging for constraining thermodynamic states during the implosion, mitigating previous issues of characterization. By revealing regions of parameter space that best constrain atomic models, this framework can extract the elusive microphysics that dictates the nature of matter at extreme pressures.

Acknowledgements

This material is based upon work supported by the Department of Energy National Nuclear Security Administration under Award Number DE-NA0003856, the University of Rochester, and the New York State Energy Research and Development Authority, and under the auspices of the U.S. Department of Energy by Lawrence Livermore National Laboratory under Contract DEAC52-07NA27344. Partial funding for this research was provided by the Center for Matter at Atomic Pressures (CMAP), a National Science Foundation (NSF) Physics Frontier Center, under Award PHY-2020249. D.A.C. acknowledges the DOE NNSA SSGF support, which is provided under Cooperative Agreement No. DE-NA0003960.

This report was prepared as an account of work sponsored by an agency of the U.S. Government. Neither the U.S. Government nor any agency thereof, nor any of their employees, makes any warranty, express or implied, or assumes any legal liability or responsibility for the accuracy, completeness, or usefulness of any information, apparatus, product, or process disclosed, or represents that its use would not infringe privately owned rights. Reference herein to any specific commercial product, process, or service by trade name, trademark, manufacturer, or otherwise does not necessarily constitute or imply its endorsement, recommendation, or favoring by the U.S. Government or any agency thereof. The views and opinions of authors expressed herein do not necessarily state or reflect those of the U.S. Government or any agency thereof.

Appendix A. Screened Hydrogenic model

The screened hydrogenic model is a computationally inexpensive atomic model for estimating material and radiative properties of any ionization state of any element [6, 29, 30]. Correlations between bound electrons are treated through a screening matrix. The screening matrix σ_{ij} describes how the i^{th} electron reduces the effective nuclear charge acting on the j^{th} electron. Hydrogenic equations modified by the screening are employed to calculate level energies, oscillator strengths, excitation rates, and other atomic data. The model is

approximate yet computationally inexpensive. Due to its simplicity, the model can be modified and applied to a range of problems.

The screened-hydrogenic average-ion model conceives a fictitious ion of fractional charge and fractional shell populations, representing the average quantum state of all ions in the plasma. Plasma effects are introduced by allowing shell populations P_n to fluctuate in response to a prescribed temperature T and density ρ. Dense plasma effects can be included through ionization potential depression.

To initiate the model, mass density ρ, temperature T, and a trial mean ionization state $\bar{Z}$ are given. These are used to calculate the chemical potential μ of the plasma, the ionization potential depression ΔE_c (IPD), and a pressure-induced occupation factor g_n. Next, g_n is solved self-consistently with Fermi-distributed shell populations P_n, the screened nuclear charges Q_n, and orbital radii R_n. The energy levels E_n are determined self-consistently with P_n, Q_n, and W_n. The mean ionization state $\bar{Z}$ can then be calculated by summing over the P_n of bound levels, defined as the levels having $E_n + \Delta E_c > 0$. This entire loop must be iterated to achieve convergence between the trial $\bar{Z}$ and the calculated $\bar{Z}$. Definitions and equations are shown in Table A.2, and a graph of the workflow is shown in Fig. A.7.

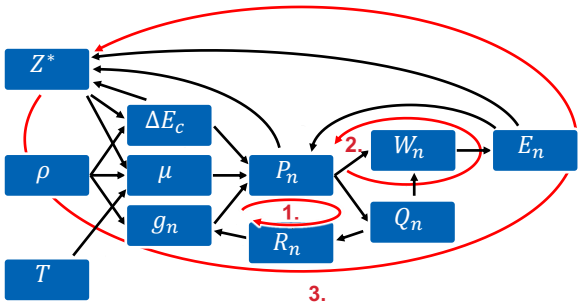

Figure A.7: Average ion workflow. Black arrows indicate dependencies. Red arrows indicate recursive loops requiring a self-consistent solution. The red arrow begins and ends on the quantity requiring iteration. The order in which the self-consistent loops should be performed is noted by the red numbers. See Table A.2 for equations.

A consequence of coupling the atom to the plasma environment is that $\bar{Z}$ has no closed form solution. A self-consistent solution must be found by iterating over circularly dependent equations until the calculated value equals the input value to within some tolerance. There are three quantities that require such solution: (1) g_n by iterating over $g_n - P_n - Q_n - R_n$, (2) P_n by iterating over $P_n - Q_n - W_n - E_n$, and (3) $\bar{Z}$ by iterating over the entire calculation. If the difference in calculated and input values of some quantity f exceeds the user-specified tolerance for any of these loops, the new input value f^{new}_{input} is taken as a linear mixing of the previous input value f^{old}_{input} and the calculated value f^{old}_{calc}:

$$f^{new}_{input} = (1 - c) \times f^{old}_{input} + c \times f^{old}_{calc}. \qquad \text{(A.1)}$$

Values of the mixing coefficient $c \in (0, 1)$ are chosen to aid convergence. Values near 0.5 tend to be optimal. Through inclusion of μ, ΔE_c, and g_n, this model approximates the impact of the dense plasma environment on P_n and $\bar{Z}$. The screened hydrogenic model used for all relevant calculations in this paper has been made available [45].

References

[1] Frontiers for discovery in high energy density science, prepared for the Office of Science and Technology Policy, National Science and Technology Council Interagency Working Group on the Physics of the Universe and prepared by the National Task Force on High Energy Density Physics (20 July 2004).

[2] X. Li, F. B. Rosmej, Quantum-number-dependent energy level shifts of ions in dense plasmas: A generalized analytical approach, Europhys. Lett. 99 (2012) 33001. doi:10.1209/0295-5075/99/33001.

[3] D. L. Foulis, S. J. Rose, T. D. Beynon, Transient multi-centre electronic structure in dense plasmas, J. Quant. Spectrosc. Radiat. Transf. 58 (1997) 577–583. doi:10.1016/S0022-4073(97)00064-2.

[4] S. J. Rose, D. L. Foulis, P. Gauthier, The effect of transient molecules on the bound-bound contribution to the radiative opacity at the centre of the Sun, J. Phys. B At. Mol. Opt. Phys. 31 (1998) L127 – L133. doi:10.1088/0953-4075/31/4/003.

[5] S. X. Hu, V. V. Karasiev, V. Recoules, P. M. Nilson, N. Brouwer, M. Torrent, Interspecies radiative transition in warm and super-dense plasma mixtures, Nat. Commun. 11 (2020) 1989. doi:10.1038/s41467-020-15916-3.

[6] S. Atzeni, J. Meyer-ter Vehn, The Physics of Inertial Fusion : Beam Plasma Interaction, Hydrodynamics, Hot Dense Matter, 1st Edition, International Series of Monographs on Physics, vol. 125, Oxford University Press, Oxford, United Kingdom, 2004.

[7] E. Moravveji, The impact of enhanced iron opacity on massive star pulsations: Updated instability strips, Mon. Not. R. Astron. Soc. 455 (2016) L67–L71. doi:10.1093/mnrasl/slv142.

[8] J. Daszyńska-Daszkiewicz, P. Walczak, A. Pamyatnykh, W. Szewczuk, Testing stellar opacities using asteroseismology, arXiv 10 (2019) 136–141. arXiv:1912.00409, doi:10.48550/arXiv.1912.00409.

[9] M. Le Pennec, S. Turck-Chièze, S. Salmon, C. Blancard, P. Cossé, G. Faussurier, G. Mondet, First new solar models with opas opacity tables, Astrophys. J. Lett. 813 (2015) L42. doi:10.1088/2041-8205/813/2/L42.

[10] S. M. Vinko, O. Ciricosta, B. I. Cho, K. Engelhorn, H. K. Chung, C. R. Brown, T. Burian, J. Chalupský, R. W. Falcone, C. Graves, V. Hájková, A. Higginbotham, L. Juha, J. Krzywinski, H. J. Lee, M. Messerschmidt, C. D. Murphy, Y. Ping, A. Scherz, W. Schlotter, S. Toleikis, J. J. Turner, L. Vysin, T. Wang, B. Wu, U. Zastrau, D. Zhu, R. W. Lee, P. A. Heimann,

Table A.2: Quantities and equations used in the average ion model.

Quantity	Symbol	Equation
Ionization potential depression (IPD)	ΔE_c	See Eq. 3
Chemical potential	μ	$k_B T\left[-\frac{3}{2}\ln\Theta + \ln\frac{4}{3\sqrt{\pi}} + \frac{A\Theta^{-(b+1)}+B\Theta^{-(b+1)/2}}{1+A\Theta^{-b}}\right]$ $A = 0.250254, \quad B = 0.072, \quad b = 0.858$
Degeneracy parameter	Θ	T/T_F
Pressure-induced occupation factor	g_n	$\frac{2n^2}{1+\left(a\frac{R_n}{R_0}\right)^b}$
Ion-sphere radius	R_0	$\left(\frac{3Am_p}{4\pi\rho}\right)^{1/3}$
Fermi-distributed shell populations	P_n	$\frac{g_n}{1+\exp\left[\frac{E_n+\Delta E_c-\mu}{k_B T}\right]}$
Effective nuclear charge at n^{th} shell	Q_n	$Z - \sum_{m\le n}\sigma_{nm}P_m$
Shell radius	R_n	$a_0\frac{n^2}{Q_n}$
Screening of n^{th} shell by outer electrons	W_n	$\sum_{m\ge n}\frac{P_m Q_m}{m^2}\sigma_{mn}$
Energy of n^{th} shell	E_n	$E_A\left(W_n - \frac{Q_n^2}{2n^2}\right)$
Mean ionization state	$\bar{Z}$	$Z - \sum_n P_n$, sum over bound states n having $E_n + \Delta E_c > 0$

B. Nagler, J. S. Wark, Creation and diagnosis of a solid-density plasma with an X-ray free-electron laser, Nature 482 (2012) 59–62. doi:10.1038/nature10746.

[11] D. J. Hoarty, P. Allan, S. F. James, C. R. Brown, L. M. Hobbs, M. P. Hill, J. W. Harris, J. Morton, M. G. Brookes, R. Shepherd, J. Dunn, H. Chen, E. Von Marley, P. Beiersdorfer, H. K. Chung, R. W. Lee, G. Brown, J. Emig, Observations of the effect of ionization-potential depression in hot dense plasma, Phys. Rev. Lett. 110 (2013) 265003. doi:10.1103/PhysRevLett.110.265003.

[12] O. Ciricosta, S. M. Vinko, H. K. Chung, B. I. Cho, C. R. Brown, T. Burian, J. Chalupský, K. Engelhorn, R. W. Falcone, C. Graves, V. Hájková, A. Higginbotham, L. Juha, J. Krzywinski, H. J. Lee, M. Messerschmidt, C. D. Murphy, Y. Ping, D. S. Rackstraw, A. Scherz, W. Schlotter, S. Toleikis, J. J. Turner, L. Vysin, T. Wang, B. Wu, U. Zastrau, D. Zhu, R. W. Lee, P. Heimann, B. Nagler, J. S. Wark, Direct measurements of the ionization potential depression in a dense plasma, Phys. Rev. Lett. 109 (2012) 065002. doi:10.1103/PhysRevLett.109.065002.

[13] D. S. Montgomery, W. S. Daughton, B. J. Albright, A. N. Simakov, D. C. Wilson, E. S. Dodd, R. C. Kirkpatrick, R. G. Watt, M. A. Gunderson, E. N. Loomis, E. C. Merritt, T. Cardenas, P. Amendt, J. L. Milovich, H. F. Robey, R. E. Tipton, M. D. Rosen, Design considerations for indirectly driven double shell capsules, Phys. Plasmas 25 (2018) 092706. doi:10.1063/1.5042478.

[14] L. B. Fletcher, A. L. Kritcher, A. Pak, T. Ma, T. Döppner, C. Fortmann, L. Divol, O. S. Jones, O. L. Landen, H. A. Scott, J. Vorberger, D. A. Chapman, D. O. Gericke, B. A. Mattern, G. T. Seidler, G. Gregori, R. W. Falcone, S. H. Glenzer, Observations of continuum depression in warm dense matter with X-ray thomson scattering, Phys. Rev. Lett. 112 (2014) 145005. doi:10.1103/PhysRevLett.112.145004.

[15] O. Ciricosta, S. M. Vinko, B. Barbrel, D. S. Rackstraw, T. R. Preston, T. Burian, J. Chalupský, B. I. Cho, H. K. Chung, G. L. Dakovski, K. Engelhorn, V. Hájková, P. Heimann, M. Holmes, L. Juha, J. Krzywinski, R. W. Lee, S. Toleikis, J. J. Turner, U. Zastrau, J. S. Wark, Measurements of continuum lowering in solid-density plasmas created from elements and compounds, Nat. Commun. 7 (2016) 11713. doi:10.1038/ncomms11713.

[16] S. B. Hansen, E. C. Harding, P. F. Knapp, M. R. Gomez, T. Nagayama, J. E. Bailey, Changes in the electronic structure of highly compressed iron revealed by X-ray fluorescence lines and absorption edges, High Energy Density Phys. 24 (2017) 39–43. doi:10.1016/j.hedp.2017.07.002.
URL http://dx.doi.org/10.1016/j.hedp.2017.07.002

[17] J. J. Ruby, J. R. Rygg, D. A. Chin, J. A. Gaffney, P. J. Adrian, D. Bishel, C. J. Forrest, V. Y. Glebov, N. V. Kabadi, P. M. Nilson, Y. Ping, C. Stoeckl, G. W. Collins, Constraining physical models at gigabar pressures, Phys. Rev. E 102 (2020) 53210. doi:10.1103/PhysRevE.102.053210.
URL https://doi.org/10.1103/PhysRevE.102.053210

[18] J. J. Ruby, J. R. Rygg, D. A. Chin, J. A. Gaffney, P. J. Adrian, C. J. Forrest, V. Y. Glebov, N. V. Kabadi, P. M. Nilson, Y. Ping, C. Stoeckl, G. W. Collins, Energy Flow in Thin Shell Implosions and Explosions, Phys. Rev. Lett. 125 (2020) 215001. doi:10.1103/PhysRevLett.125.215001.
URL https://doi.org/10.1103/PhysRevLett.125.215001

[19] J. C. Stewart, K. D. Pyatt, Lowering of Ionization Potentials in Plasmas, Astrophys. J. 144 (1966) 1203–1211.

[20] G. Ecker, W. Kröll, Lowering of the ionization energy for a plasma in thermodynamic equilibrium, Phys. Fluids 6 (1963) 62–69. doi:10.1063/1.1724509.

[21] J. Delettrez, R. Epstein, M. C. Richardson, P. A. Jaanimagi, B. L. Henke, Effect of laser illumination nonuniformity on the analysis of time-resolved x-ray measurements in uv spherical transport experiments, Phys. Rev. A 36 (1987) 3926–3934. doi:10.1103/PhysRevA.36.3926.

[22] N. H. Magee Jr., R. Clark, Los Alamos opacity web page, Con-

ference: 1. International Conference on Atomic and Molecular Data and Their Standards (LA-UR-97-4606) (1998) 4–7.
URL https://www.osti.gov/biblio/645556

[23] B. J. Crowley, Continuum lowering - A new perspective, High Energy Density Phys. 13 (2014) 84–102. doi:10.1016/j.hedp.2014.04.003.
URL http://dx.doi.org/10.1016/j.hedp.2014.04.003

[24] S. X. Hu, Continuum lowering and fermi-surface rising in strongly coupled and degenerate plasmas, Phys. Rev. Lett. 119 (2017) 065001. doi:10.1103/PhysRevLett.119.065001.

[25] S. M. Vinko, O. Ciricosta, J. S. Wark, Density functional theory calculations of continuum lowering in strongly coupled plasmas, Nat. Commun. 5 (2014) 3533. doi:10.1038/ncomms4533.

[26] G. Faussurier, C. Blancard, Density effects on electronic configurations in dense plasmas, Phys. Rev. E 97 (2018) 023206. doi:10.1103/PhysRevE.97.023206.

[27] J. Toulouse, Review of approximations for the exchange-correlation energy in density-functional theory, (2021). arXiv:2103.02645v2.

[28] H. R. Griem, Principles of Plasma Spectroscopy, Cambridge Monographs on Plasma Physics, Cambridge University Press, 1997. doi:10.1017/CBO9780511524578.

[29] H. Mayer, Methods of opacity calculations, Atomic Energy Commission Reports, Los Alamos Scientific Laboratory, Los Alamos, NM, 1949, pp. 1–151.
URL https://permalink.lanl.gov/object/tr?what=info:lanl-repo/lareport/LA-00647

[30] G. B. Zimmerman, R. M. More, Pressure ionization in laser-fusion target simulation, J. Quant. Spectrosc. Radiat. Transf. 23 (1980) 517–522. doi:10.1016/0022-4073(80)90055-2.

[31] S. B. Hansen, A. Y. Faenov, T. A. Pikuz, K. B. Fournier, R. Shepherd, H. Chen, K. Widmann, S. C. Wilks, Y. Ping, H. K. Chung, A. Niles, J. R. Hunter, G. Dyer, T. Ditmire, Temperature determination using Kα spectra from M-shell Ti ions, Phys. Rev. E 72 (2005) 036408. doi:10.1103/PhysRevE.72.036408.

[32] A. Hauer, R. D. Cowan, B. Yaakobi, O. Barnouin, R. Epstein, Absorption-spectroscopy diagnosis of pusher conditions in laser-driven implosions, Phys. Rev. A 34 (1986) 411–420. doi:10.1103/PhysRevA.34.411.

[33] H. M. Johns, R. C. Mancini, P. Hakel, T. Nagayama, V. A. Smalyuk, S. P. Regan, J. Delettrez, Compressed shell conditions extracted from spectroscopic analysis of Ti K-shell absorption spectra with evaluation of line self-emission, Phys. Plasmas 21 (2014). doi:10.1063/1.4892554.
URL http://dx.doi.org/10.1063/1.4892554

[34] L. A. Pickworth, B. A. Hammel, V. A. Smalyuk, M. Hoppe, B. Haid, M. Dayton, H. F. Robey, C. Walters, H. A. Scott, S. P. Regan, T. Kohut, A. G. MacPhee, M. B. Schneider, M. A. Barrios, O. L. Landen, D. Holunga, Measurement of Hydrodynamic Growth near Peak Velocity in an Inertial Confinement Fusion Capsule Implosion using a Self-Radiography Technique, Phys. Rev. Lett. 117 (2016) 035001. doi:10.1103/physrevlett.117.035001.

[35] S. X. Hu, D. T. Bishel, D. A. Chin, P. M. Nilson, V. V. Karasiev, I. E. Golovkin, M. Gu, S. B. Hansen, D. I. Mihaylov, N. R. Shaffer, S. Zhang, T. Walton, Probing atomic physics at ultra-high pressure using laser-driven implosions, Nat. Commun. 13 (2022) 6780. doi:10.1038/s41467-022-34618-6.

[36] D. E. Fratanduono, T. R. Boehly, P. M. Celliers, M. A. Barrios, J. H. Eggert, R. F. Smith, D. G. Hicks, G. W. Collins, D. D. Meyerhofer, The direct measurement of ablation pressure driven by 351-nm laser radiation, J. Appl. Phys. 110 (2011) 073110. doi:10.1063/1.3646554.

[37] R. Epstein, T. J. B. Collins, J. A. Delettrez, S. Skupsky, R. P. J. Town, Simulation of the Radiative Preheat of Target Foils and Shells in Laser-Driven Ablation and Implosion Experiments, in: 40th Annu. Meet. APS Div. Plasma Phys., American Physical Society, New Orleans, LA, 1998.
URL https://flux.aps.org/meetings/YR98/BAPSDPP98/abs/S1100010.html

[38] R. Florido, R. C. Mancini, T. Nagayama, R. Tommasini, J. A. Delettrez, S. P. Regan, B. Yaakobi, Measurements of core and compressed-shell temperature and density conditions in thick-wall target implosions at the OMEGA laser facility, Phys. Rev. E 83 (2011) 066408. doi:10.1103/PhysRevE.83.066408.

[39] S. P. Regan, R. Epstein, B. A. Hammel, L. J. Suter, H. A. Scott, M. A. Barrios, D. K. Bradley, D. A. Callahan, C. Cerjan, G. W. Collins, S. N. Dixit, T. Döppner, M. J. Edwards, D. R. Farley, K. B. Fournier, S. Glenn, S. H. Glenzer, I. E. Golovkin, S. W. Haan, A. Hamza, D. G. Hicks, N. Izumi, O. S. Jones, J. D. Kilkenny, J. L. Kline, G. A. Kyrala, O. L. Landen, T. Ma, J. J. Macfarlane, A. J. Mackinnon, R. C. Mancini, R. L. McCrory, N. B. Meezan, D. D. Meyerhofer, A. Nikroo, H. S. Park, J. Ralph, B. A. Remington, T. C. Sangster, V. A. Smalyuk, P. T. Springer, R. P. Town, Hot-spot mix in ignition-scale inertial confinement fusion targets, Phys. Rev. Lett. 111 (4) (2013) 1–5. doi:10.1103/PhysRevLett.111.045001.

[40] O. Ciricosta, H. Scott, P. Durey, B. A. Hammel, R. Epstein, T. R. Preston, S. P. Regan, S. M. Vinko, N. C. Woolsey, J. S. Wark, Simultaneous diagnosis of radial profiles and mix in NIF ignition-scale implosions via X-ray spectroscopy, Phys. Plasmas 24 (2017) 112703. doi:10.1063/1.5000774.
URL http://dx.doi.org/10.1063/1.5000774

[41] J. J. MacFarlane, I. E. Golovkin, P. R. Woodruff, D. R. Welch, B. V. Oliver, T. A. Mehlhorn, R. B. Campbell, Simulation of the ionization dynamics of aluminum irradiated by intense short-pulse lasers, in: B. A. Hammel, D. D. Meyerhofer, J. Meyer-ter Vehn, H. Azechi (Eds.), Inert. Fusion Sci. Appl. 2003, American Nuclear Society, La Grange Park, IL, 2003, pp. 457–460.
URL http://www.prism-cs.com/Software/PrismSPECT/AlumIonizDynamics.pdf

[42] D. Sivia, J. Skilling, Data Analysis: A Bayesian Tutorial, 2nd Edition, Oxford University Press, Oxford, United Kingdom, 2006. doi:10.48550/arXiv.1810.09538.

[43] D. Phan, N. Pradhan, M. Jankowiak, Composable effects for flexible and accelerated probabilistic programming in numpyro, arXiv preprint arXiv:1912.11554 (2019).

[44] E. Bingham, J. P. Chen, M. Jankowiak, F. Obermeyer, N. Pradhan, T. Karaletsos, R. Singh, P. Szerlip, P. Horsfall, N. D. Goodman, Pyro: Deep universal probabilistic programming, J. Mach. Learn. Res. 20 (2019) 1–6. arXiv:1810.09538.

[45] D. T. Bishel, AtPhys: Atomic Physics Package (Oct 2023). doi:https://doi.org/10.5281/zenodo.10045187.